LAWRENCE
LIVERMORE
NATIONAL
LABORATORY

UCRL-TR-230332

Electrochemical Studies of Passive Film Stability on Fe48Mo14Cr15Y2C15B Amorphous Metal in Seawater at 90oC and 5M CaCl2 at 105oC

J.C. Farmer, S.D. Day, T. Lian, C.K. Saw, P.D. Hailey, C.A. Blue, W. Peters, J.H. Payer, J.H. Perepezko, K.Hildal, D.J. Branagan, E.J. Buffa, L. Aprigliano

April 27, 2007

This work was performed under the auspices of the U.S. Department of Energy by University of California, Lawrence Livermore National Laboratory under Contract W-7405-Eng-48

Electrochemical Studies of Passive Film Stability on $Fe_{48}Mo_{14}Cr_{15}Y_2C_{15}B$ Amorphous Metal in Seawater at 90°C and 5M $CaCl_2$ at 105°C

J. C. Farmer, S. D. Day, T. Lian, C. K. Saw, & P. D. Hailey
Lawrence Livermore National Laboratory, Livermore, California

C. A. Blue & W. Peters
Oak Ridge National Laboratory, Oak Ridge, Tennessee

J. H. Payer
Case Western Reserve University, Cleveland, Ohio

J. H. Perepezko and K. Hildal
University of Wisconsin, Madison, Wisconsin

D. J. Branagan and E. J. Buffa
The NanoSteel Company, Idaho Falls, Idaho

L. F. Aprigliano
Strategic Analysis, Arlington, Virginia

Several Fe-based amorphous metal formulations have been identified that appear to have corrosion resistance comparable to, or better than that of Ni-based Alloy C-22 (UNS # N06022), based on measurements of breakdown potential and corrosion rate in seawater. Both chromium (Cr) and molybdenum (Mo) provide corrosion resistance, boron (B) enables glass formation, and rare earths such as yttrium (Y) lower critical cooling rate (CCR). Amorphous $Fe_{48.0}Cr_{15.0}Mo_{14.0}B_{6.0}C_{15.0}Y_{2.0}$ (SAM1651) has a low critical cooling rate (CCR) of less than 80 Kelvin per second, due to the addition of yttrium. The low CCR enables it to be rendered as a completely amorphous material in practical materials processes. While the yttrium enables a low CCR to be achieved, it makes the material relatively difficult to atomize, due to increases in melt viscosity. Consequently, the powders produced thus far have had irregular shape, which had made pneumatic conveyance during thermal spray deposition difficult.

I. INTRODUCTION

The outstanding corrosion that may be possible with amorphous metals has been recognized for many years [1-4]. Compositions of several iron-based amorphous metals have been published, including several with very good corrosion resistance. Examples include: thermally sprayed coatings of Fe-10Cr-10-Mo-(C,B), bulk Fe-Cr-Mo-C-B, and Fe-Cr-Mo-C-B-P [5-7]. Another family of iron-based amorphous metals with very good corrosion resistance has been developed that can be applied as a protective thermal spray coatings. One of the most promising formulations within this family is $Fe_{49.7}Cr_{17.7}Mn_{1.9}Mo_{7.4}W_{1.6}B_{15.2}C_{3.8}Si_{2.4}$ (SAM2X5), which includes chromium (Cr), molybdenum (Mo), and tungsten (W) for enhanced corrosion resistance, and boron (B) to enable glass formation and neutron absorption [8-12]. Several nickel-based amorphous metals have also been developed that exhibit exceptional corrosion performance in acids [13]. Very good thermal spray coatings of nickel-based crystalline coatings have been deposited with thermal spray, but appear to have less corrosion resistance than the nickel-based amorphous metals [14].

A detailed study of the corrosion resistance of $Fe_{48}Mo_{14}Cr_{15}Y_2C_{15}B_6$ (SAM1651) in 5M $CaCl_2$ at 105°C, and in natural seawater at 30 and 90°C is discussed here. Yttrium is added to this amorphous alloy to achieve a very low critical cooling rate of approximately 80 Kelvin per second. SAM1651 has the same nominal elemental composition as the Y-containing Fe-based amorphous metal formulation discussed in the literature [15-19]. The target compositions of this alloy, other amorphous alloys in the same family, Type 316L austenitic stainless steel (UNS # S31603) and nickel-based Alloy C-22 (UNS # N06022) are given in Table I.

The exceptional passive film stability and corrosion resistance of these iron-based amorphous alloys were based on measurements of the passive film breakdown and potential, measurements of corrosion rate and performance during salt fog testing. Such measurements enable the corrosion performances various iron-based amorphous alloys, carbon steel, Type 316L stainless steel, and Alloy C-22 to be directly compared. Spontaneous breakdown of the passive film and localized corrosion require that the open-circuit corrosion potential exceed the critical potential:

$$E_{corr} \geq E_{critical} \quad (1)$$

The resistance to localized corrosion is quantified through measurement of the open-circuit corrosion potential (E_{corr}), the breakdown potential ($E_{critical}$) and the repassivation potential (E_{rp}). The greater the difference between the open-circuit corrosion potential and the repassivation potential (ΔE), the more resistant a material is to modes of localized corrosion such a pitting and crevice corrosion. In integrated corrosion models, general corrosion is invoked when E_{corr} is less than $E_{critical}$ ($E_{corr} < E_{critical}$), and localized corrosion is invoked when E_{corr} exceeds $E_{critical}$ [20].

In the published scientific literature, different bases exist for determining the critical potential from electrochemical measurements [21-22]. The critical or threshold potential is frequently defined as the potential where the passive current density increases to a level between 1 to 10 $\mu A/cm^2$ (10^{-6} to 10^{-5} A/cm^2) while positively increasing potential during cyclic polarization or potential-step testing. The repassivation potential is defined as the point during cyclic polarization where the current density drops to a level indicative of passivity, which is *assumed* to be between 0.1 to 1.0 $\mu A/cm^2$ (10^{-6} to 10^{-7} A/cm^2). An alternative definition of the repassivation potential is the point during cyclic polarization where the forward and reverse

scans intersect, a point where the current density being measured during the reverse scan drops to a level *known* to be indicative of passivity. Details are discussed in the subsequent section.

II. EXPERIMENTAL

A. Melt Spinning Process

Maximum cooling rates of one million Kelvin per second (10^6 K/s) have been achieved with melt spinning, which is an ideal process for producing amorphous metals over a very broad range of compositions. This process was used to synthesize completely amorphous, Fe-based, corrosion-resistant alloys with near theoretical density, and thereby enabled the effects of coating morphology on corrosion resistance to be separated from the effects of elemental composition. The melt-spun ribbon (MSR) samples produced with this equipment were several meters long, several millimeters wide and approximately 150 microns thick.

B. Thermal Spray Process

The coatings discussed here were made with the high-velocity oxy-fuel (HVOF) process with characteristic gas and particle velocities that were three to four times the speed of sound (mach 3 to 4). This process was ideal for depositing metal and cermet coatings, which had typical bond strengths of 5,000 to 10,000 pounds per square inch (5-10 ksi), porosities of less than one percent (< 1%), and extreme hardness. The cooling rate that can be achieved with HVOF is on the order of ten thousand Kelvin per second (10^4 K/s), and was high enough to enable many alloy compositions to be deposited above their respective critical cooling rate, thereby maintaining the vitreous state. However, the range of amorphous metal compositions that can be processed with HVOF is more restricted than those that can be produced with melt spinning, due to the differences in achievable cooling rates. Both kerosene and hydrogen have been investigated as fuels in the HVOF process used to deposit SAM2X5.

C. Energy Dispersive Spectroscopy

The target concentrations of heavier elements such as Cr, Mo and W were verified with Energy Dispersive Spectroscopy (EDS). Microanalysis of each sample was performed at three randomly selected locations at 10,000X magnification. Compositional analysis was performed on the smoother side of each melt-spun ribbon (MSR), as the rougher sides were found in some cases to be contaminated with small amounts of copper, presumably from contact with the copper wheel during the melt spinning process. The concentrations of relatively light elements such as B and C could not be determined with EDS, and were therefore estimated with a simple difference calculation, so that the sum of concentrations for all elements totaled one hundred percent.

D. X-Ray Diffraction

The basic theory for X-ray diffraction (XRD) of amorphous materials is well developed and has been published in the literature [23-24]. In an amorphous material, there are broad diffraction peaks. During this study, XRD was done with CuK_α X-rays, a graphite analyzing crystal, and a Philips vertical goniometer, using the Bragg-Bretano method. The X-ray optics were self-focusing, and the distance between the X-ray focal point to the sample position was equal to the distance between the sample position and the receiving slit for the reflection mode. Thus, the intensity and resolution was optimized. Parallel vertical slits were added to improve the scattering signal. Step scanning was performed from 20 to 90° (2θ) with a step size of 0.02° at 4

to 10 seconds per point, depending on the amount of sample. The samples were loaded into low-quartz holder since the expected intensity was very low, thus requiring that the background scattering be minimized.

E. Thermal Analysis

The thermal properties of these Fe-based amorphous metals were also determined. Thermal analysis of these Fe-based amorphous metals, done with differential scanning calorimetry (DSC) or differential thermal analysis (DTA), allowed determination of important thermal properties such as the glass transition temperature (T_g), crystallization temperature (T_x), and the melting point (T_m). Results from the thermal analysis of amorphous samples provides initial assessment of the glass forming ability of these materials through conventional metrics, such as the reduced glass transition temperature ($T_{rg} = T_g/T_L$).

F. Mechanical Properties

Hardness was measured, since it determines wear resistance, as well as resistance to erosion-corrosion. Vickers micro-hardness (HV) was the standard approach used to assess the hardness of these thermal spray coatings. A 300-gram load was used since it was believed that this load and the affected area were large enough to sample across any existing macro-porosity, thereby producing a spatially averaged measurement. Micro-hardness measurements were also made with a 100-gram load since it was believed that this load and the affected area were small enough to accurately sample bulk material properties.

G. Cyclic Polarization

Cyclic polarization (CP) measurements were based on a procedure similar to ASTM (American Society for Testing and Materials) G-5 and other similar standards, with slight modification [25-28]. The ASTM G-5 standard calls for a 1N H_2SO_4 electrolyte, whereas synthetic bicarbonate, sulfate-chloride, chloride-nitrate, and chloride-nitrate solutions, with sodium, potassium and calcium cations, as well as natural seawater were used for this investigation. The natural seawater used in these tests was obtained directly from Half Moon Bay along the northern coast of California. Furthermore, the ASTM G-5 standard calls for the use of de-aerated solutions, whereas aerated and de-aerated solutions were used here. In regard to current densities believed to be indicative of passivity, all data was interpreted in a manner consistent with the published literature [20-22].

Temperature-controlled borosilicate glass (Pyrex) electrochemical cells were used for cyclic polarization and other similar electrochemical measurements. This cell had three electrodes, a working electrode (test specimen), a reference electrode, and a counter electrode. A standard silver silver-chloride electrode, filled with near-saturation potassium chloride solution, was used as the reference, and communicated with the test solution via a Luggin probe placed in close proximity to the working electrode, which minimized Ohmic losses. The electrochemical cell was equipped with a water-cooled junction to maintain reference electrode at ambient temperature, which thereby maintained integrity of the potential measurement, and a water-cooled condenser, which prevented the loss of volatile species from the electrolyte.

To assess the sensitivity of these iron-based amorphous metals to devitrification, which can occur at elevated temperature, melt-spun ribbons of Fe-based amorphous metals were intentionally devitrified by heat treating them at various temperatures for one hour. After heat treatment, the samples were evaluated in low temperature seawater (30°C) with cyclic

polarization, to determine the impact of the heat treatment on passive film stability and corrosion resistance. The temperatures used for the heat treatment were: 150, 300, 800 and 1000°C. Corrosion resistance was maintained below the crystallization temperature, and lost after prolonged aging at higher temperatures.

H. Potentiostatic Polarization

Potential step tests were used to determine the potential at which the passive film breaks down on $Fe_{49.7}Cr_{17.7}Mn_{1.9}Mo_{7.4}W_{1.6}B_{15.2}C_{3.8}Si_{2.4}$ (SAM2X5) and the reference material, nickel-based Alloy C-22. During prolonged periods at a constant applied potential, which were typically 24 hours in duration, the current was monitored as a function of time. In cases where passivity was lost, the current increased, and the test sample was aggressively attacked. In cases where passivity was maintained, the current decayed to a relatively constant asymptotic level, consistent with the known passive current density. In these tests, periods of polarization were preceded by one hour at the open circuit corrosion potential. To eliminate the need for surface roughness corrections in the conversion of measured current and electrode area to current density, the SAM2X5 coatings were polished to a 600-grit finish prior to testing. The constant potential denoted in the figures was applied after 1 hour at the open circuit corrosion potential (OCP).

I. Linear Polarization

The linear polarization method was used as a method for determining the corrosion rates of the various amorphous metal coatings. The procedure used for linear polarization testing consisted of the following steps: (1) holding the sample for ten seconds at the OCP; (2) beginning at a potential 20 mV below the OCP, increasing the potential linearly at a constant rate of 0.1667 mV per second to a potential 20 mV above the OCP; (3) recording the current being passed from the counter electrode to the working electrode as a function of potential relative to a standard Ag/AgCl reference electrode; and (4) determining the parameters in the cathodic Tafel line by performing linear regression on the voltage-current data, from 10 mV below the OCP, to 10 mV above the OCP. The slope of this line was the polarization resistance, *Rp* (ohms), and was defined in the published literature [29]. While no values for the Tafel parameter (*B*) of Fe-based amorphous metals have yet been developed, it was believed that a conservative value of approximately 25 mV was reasonable, based upon the range of published values for several Fe- and Ni-based alloys. The corrosion current density was then defined in terms of *B*, R_p and *A*, the actual exposed area of the sample being tested. The general corrosion rate was calculated from the corrosion current density through application of Faraday's Law [30]:

$$R_P = \left(\frac{\partial E}{\partial I} \right)_{E_{corr}} \tag{2}$$

A parameter (*B*) were defined in terms of the slopes of the anodic and cathodic branches of the Tafel line:

$$B = \frac{\beta_a \beta_c}{2.303(\beta_a + \beta_c)} \tag{3}$$

Values of B were published for a variety of iron-based alloys, and varied slightly from one alloy-environment combination to another [29]. Values for carbon steel, as well as Type 304, 304L and 430 stainless steels, in a variety of electrolytes which include seawater, sodium chloride, and sulfuric acid, ranged from 19 to 25 mV. A value for nickel-based Alloy 600 in lithiated water at 288°C was given as approximately 24 mV. While no values have yet been developed for the Fe-based amorphous metals that were the subject of this investigation, it was believed that a conservative representative value of approximately 25 mV was appropriate for the conversion of polarization resistance to corrosion current. Given the value for Alloy 600, a value of 25 mV was also believed to be acceptable for converting the polarization resistance for nickel-based Alloy C-22 to corrosion current. The corrosion current, I_{corr} (A) was then defined as:

$$I_{corr} = \frac{B}{R_p} \tag{4}$$

The parameter B was conservatively assumed to be approximately 25 mV. The corrosion current density, i_{corr} (A cm^{-2}), was defined as the corrosion current, normalized by electrode area, and was:

$$i_{corr} = \frac{I_{corr}}{A} \tag{5}$$

A was the surface area of the sample in square centimeters (cm^2). The corrosion (or penetration) rates of the amorphous alloy and reference materials were calculated from the corrosion current densities with the following formula, which was similar to that given by Jones [30]:

$$\frac{dp}{dt} = \frac{i_{corr}}{\rho_{alloy} n_{alloy} F} \tag{6}$$

where p was the penetration depth, t was time, i_{corr} was the corrosion current density, ρ_{alloy} was the density of the alloy (g cm^{-3}), n_{alloy} was the number of gram equivalents per gram of alloy, and F was Faraday's constant. The value of n_{alloy} was calculated with the following formula:

$$n_{alloy} = \sum_j \left(\frac{f_j n_j}{a_j} \right) \tag{7}$$

where f_j was the mass fraction of the jth alloying element in the material, n_j was the number of electrons involved in the anodic dissolution process, which was assumed to be congruent, and a_j was the atomic weight of the jth alloying element. Congruent dissolution was assumed, which meant that the dissolution rate of a given alloy element was proportional to its concentration in the bulk alloy. These equations were used to calculate factors for the conversion of corrosion current density to the penetration rate (corrosion rate). These conversion factors were summarized in Table II.

J. Junction Potential Correction

It is important to understand the magnitude of the error in the potential measurements due to the junction potential. Consistent with the methods given by Bard and Faulkner, a correction was performed based upon the Henderson Equation [31]. The calculated junction potentials for several test solutions were estimated with ionic properties taken from Bard and Faulkner. These corrections were not very large, with the largest being less than approximately 10 mV. It was therefore concluded that no significant error would result from neglecting the junction potential correction.

K. Salt Fog Testing

Salt fog tests were conducted according to the standard General Motors (GM) salt fog test, identified as GM9540P. The protocol for this test is summarized in Table III. The four reference samples included Type 316L stainless steel, nickel-based Alloy C-22, Ti Grade 7, and the 50:50 nickel-chromium binary.

III. EXPERIMENTAL RESULTS

A. Elemental Composition

Several Fe-based amorphous metals were systematically explored during this investigation, with the compositions of the yttrium-containing variants summarized in Table I. Additions of molybdenum (Mo), chromium (Cr) and tungsten (W) were added to enhance passivity; boron (B) was added to enable glass formation; and yttrium (Y) was added to lower critical cooling rate (CRR). SAM3X1, SAM3X3, SAM3X5 and SAM3X7 melt-spun ribbons were prepared by adding 3, 5 and 7 at. % Y to SAM40 parent alloy, respectively. Similarly, SAM8 melt-spun ribbon was prepared by adding 3 at. % W to the SAM1651 parent alloy. The compositions of melt-spun ribbon samples were verified with energy dispersive spectroscopy (EDS) and are summarized in Table IV.

Figure 1 shows X-ray diffraction (XRD) data for melt-spun ribbon (MSR) samples of Type 316L stainless steel and nickel-based Alloy C-22. The strong peaks were indicative of the crystalline nature of these materials. Figure 2 shows X-ray diffraction data for melt-spun ribbon (MSR) samples of iron-based amorphous metals identified as: (a) SAM40; (b) SAM7, which was also known as SAM1651; and (c) SAM8 were completely amorphous, as expected.

B. Thermal Stability

In contrast, the yttrium-containing $Fe_{48.0}Cr_{15.0}Mo_{14.0}B_{6.0}C_{15.0}Y_{2.0}$ (SAM1651) has a glass transition temperature of ~584°C, a crystallization temperature of ~653°C, a melting point of ~1121°C, and a reduced glass transition temperature of ~0.55. SAM3X1, which contains 1 atomic percent yttrium, has a glass transition temperature of ~560°C, a crystallization temperature of ~614°C, a melting point of ~1108°C, and a reduced glass transition temperature of ~0.52. SAM3X5, which has significantly more yttrium than SAM3X1, has a glass transition temperature of ~590°C, a crystallization temperature of ~677°C, a melting point of ~1143°C, and a reduced glass transition temperature of 0.52. Table V summarizes these thermal properties for SAM3X1 through SAM3X7, SAM1651, and SAM1651 with tungsten (SAM8).

The critical cooling rate of SAM1651 has been determined to be ≤ 80 K per second, which was significantly less than other corrosion-resistant iron-based amorphous metals such as

SAM2X5. Clearly, the yttrium additions in SAM1651 enhance glass-forming ability of these materials.

C. Mechanical Properties

The hardness numbers for SAM1651 HVOF coatings were determined by the method described in the previous section, and are summarized in Table VI. Nine samples were evaluated with the 100-gram load, and nine samples were evaluated with the 300 gram load. The average Vickers hardness number (kg mm-2) was calculated from five indentations for each sample. In the case of the 100-gram load, the value of Hv ranged from 907 to 1154 kg mm^{-2}. In the case of the 300-gram load, the average value of Hv ranged from 857 to 997 kg mm^{-2}.

D. Passive Film Stability – 5 M $CaCl_2$ at 105°C

Cyclic polarization data for a wrought prism of nickel-based Alloy C-22, a drop-cast ingot of $Fe_{48.0}Cr_{15.0}Mo_{14.0}B_{6.0}C_{15.0}Y_{2.0}$ (SAM1651), and a melt-spun ribbon of SAM8 (SAM1651 with 3 atomic percent tungsten) in 5M $CaCl_2$ at 105°C are compared in Figure 3. Both the SAM1651 and SAM8 showed passive film stability comparable to, or better than Alloy C-22. The addition of 3 at. % W to SAM1651 enhanced the passive film stability, and also yielded more ductile and damage-tolerant amorphous metal ribbons.

Current transients wee measured at various levels of constant applied potential (100 to 450 mV vs. OCP) in 5M $CaCl_2$ at 105°C, for a polished SAM1651 HVOF coating on a Type 316L stainless steel (serial number E316L475), and are shown in Figure 4. These transients were indicative of good passive film stability, which was superior to that of wrought Alloy C-22 in this very aggressive environment. To eliminate the need for surface roughness corrections in the conversion of measured current and electrode area to current density, the SAM1651 coating was polished to a 600-grit finish prior to testing. Passive film breakdown on the HVOF coating of SAM1651 occurred at an applied potential between 360 and 400 mV vs. OCP, with a clear loss of passivity at 450 mV.

Current transients were measured at various levels of constant applied potential ranging (100 to 550 mV vs. OCP) in 5M $CaCl_2$ at 105°C, for wrought Alloy C-22 (serial number CC-22 4008), and are shown in Figure 5. These transients show complete breakdown of the passive film in two potential regimes, one regime located between 300-400 mV vs. OCP (350 mV), and the second located above 500 mV vs. OCP (550 mV). Like the polished SAM1651 coating, this reference was also polished to a 600-grit finish.

Current transients were measured at various levels of constant applied potential (100 to 350 mV vs. OCP) in 5M $CaCl_2$ at 105°C, for an as-sprayed (unpolished) Alloy C-22 HVOF coating on Type 316L stainless steel (serial number E316L256), and are shown in Figure 6. This as-sprayed HVOF coating of Alloy C-22 appears to be passive at 100-150 mV vs. OCP, but has a clear loss of passivity at potentials above 200 mV vs. OCP (250-350 mV).

Potential-step testing has been performed on HVOF coatings of SAM1651 on Type 316L stainless steel (serial number E316L475) in extremely aggressive 5M $CaCl_2$ heated to 105°C, as shown in Figure 7. Tests were also performed on the reference material, Alloy C-22, in both wrought and thermally sprayed condition (serial numbers CC-22-4008 and E316L256, respectively). To eliminate the need for surface roughness corrections in the conversion of measured current and electrode area to current density, the SAM1651 coating was polished to a 600-grit finish prior to testing. The curves represent the asymptotic current density reached after 24 hours at the corresponding potential. In this series of experiments, the passive film on

wrought Alloy C-22 also commences breakdown at a potential of only 240 mV above the open circuit corrosion potential, with evidence of repassivation at potentials above 400 mV. Even with the repassivation at higher potential, the window of vulnerability between 240 to 400 mV was problematic for the reference material (Alloy C-22). Passive film breakdown on the HVOF coating of SAM1651 occurred at a significantly higher applied potential, between 360 and 400 mV, where breakdown of the passive film on thermally sprayed Alloy C-22 was virtually spontaneous. The new SAM1651 coating provides clear advantages for operation in hot concentrated chloride brines with aggressive divalent cations such as calcium.

E. Passive Film Stability – Natural Seawater at 30 and 90°C

Current transients at various levels of constant applied potential ranging from (100 to 1000 mV vs. OCP) in deaerated seawater at 90°C, for wrought nickel-based Alloy C-22 (serial number CC-22 4007), and are shown in Figure 8. These measured transients were indicative of good passive film stability at the lower applied potentials. This sample was polished to a 600-grit finish, and has a surface area of approximately one square centimeter. At 700 to 800 mV vs. OCP, the current, which was close in value to the current density, rose to a point where the material was losing passivity (greater than 10 $\mu A/cm^2$).

Current transients were measured at various levels of constant applied potential (100 to 800 mV vs. OCP) in seawater at 90°C, for a 600-grit polished SAM1651 HVOF coating on Type 316L stainless steel (serial number E316L409), and are shown in Figure 9. These measured transients were indicative of good passive-film stability, which was comparable to that of wrought Alloy C-22. To eliminate the need for surface roughness corrections in the conversion of measured current and electrode area to current density, the SAM1651 coating was polished to a 600-grit finish prior to testing. Passive film breakdown on the HVOF coating of SM1651 occurred at an applied potential between 500 and 600 mV vs. OCP, with a clear loss of passivity at 700 mV. The coating represented by this figure was one of the first known thermal spray coatings with the SAM1651 composition.

Current transients were measured at various levels of constant applied potential (100 to 500 mV vs. OCP) in seawater at 90°C, for an as-sprayed (unpolished) Alloy C-22 HVOF coating on Type 316L stainless steel (serial number E316L255), and are shown in Figure 10. These measured transients were clearly and unambiguously indicative of a loss of passivity at the highest potential level. Since this Alloy C-22 coating was tested in the as-sprayed condition, a roughness factor must be applied to convert the *apparent* current density into the *actual* current density.

Current transients were measured at various levels of constant applied potential (100 to 736 mV vs. OCP) in seawater at 90°C, for an as-sprayed (unpolished) HVOF coating of SAM1651 on a Type 316L stainless steel (serial number E316L410), and are shown in Figure 11. These measured transients were indicative of good passive-film stability, which was comparable to that of wrought Alloy C-22. Since this as-sprayed SAM1651 coating was tested in the as-sprayed condition, a roughness factor must be applied to convert the *apparent* current density into the *actual* current density. From visual inspection, it was evident that passivity was maintained at higher potentials.

Potential-step testing in deaerated seawater heated to 90°C has been performed with SAM1651 and Alloy C-22 thermal spray coatings, as well as wrought Alloy C-22, as shown in Figure 12. The natural seawater used in these tests was obtained directly from Half Moon Bay along the northern coast of California. Tests were also performed on the reference material,

Alloy C-22, in both wrought and thermally sprayed condition. To eliminate the need for surface roughness corrections in the conversion of measured current and electrode area to current density, the SAM1651 coating was polished to a 600-grit finish prior to testing. The Alloy C-22 thermal spray coating was tested in the as-sprayed condition, so a roughness factor must be applied to convert the apparent current density into actual current density. The curves represent the asymptotic current density reached after 24 hours at the corresponding potential. In this series of experiments, the passive film on wrought Alloy C-22 also commences breakdown at a potential of approximately 600 mV above the open circuit corrosion potential. Passive film breakdown on the HVOF coating of SAM1651 occurred at an applied potential between 500 and 600 mV, where breakdown occurred at approximately 400 mV for the Alloy C-22 HVOF coating. In near-boiling seawater, the passive film stability of SAM1651 was comparable to that of Alloy C-22.

F. Linear Polarization Data – Corrosion Rates

Linear polarization was used to determine the approximate corrosion rates of the thermal spray coatings of amorphous metals of interest (HVOF SAM1651 or SAM7 and other coatings) and the reference material (wrought nickel-based Alloy C-22) in three relevant environments, Seawater at two temperature levels, and in hot concentrated calcium chloride (5M $CaCl_2$ at 105°C). Values of the corrosion potential, polarization resistance, corrosion current density, and corrosion rate are summarized in Tables VII through IX, as well as Figures 13 through 15. In seawater at 30°C, the corrosion rates of HVOF SAM1651 coatings exhibited comparable to slightly higher corrosion rates than either wrought sample of Alloy C-22 (Table VII & Figure 15). As the temperature of the seawater was increased to 90°C, the corrosion rates of HVOF SAM1651 coatings exhibited comparable to slightly lower corrosion rates than either wrought sample of Alloy C-22 (Table VIII & Figure 15). In general, corrosion rates trended to higher values with increasing temperature, as expected. In calcium chloride at 105°C, the corrosion rates of HVOF SAM1651 coatings were slightly lower than that of HVOF Alloy C-22; and comparable to slightly greater than those of wrought Alloy C-22. In general, the corrosion rates observed in the hot calcium chloride (105°C) were higher than those observed in the heated seawater (90°C), which was also expected (Table IX & Figure 15).

G. Salt Fog Testing – Verification of Corrosioin Resistance

As shown in Figure 16, salt fog testing was conducted on several thermal spray coatings, including HVOF coatings of Alloy C-22, Type 316L stainless steel, SAM40 (also referred to as SAM40), SAM1651 and other amorphous-metal formulations of interest. After 13 cycles in the GM9540P salt fog test, the HVOF coatings of Type 316L stainless steel and SAM40 showed substantial corrosion. Very slight rust spots were observed on the C-22 coating. In contrast, the newer SAM1651 formulations showed no corrosion at 30 cycles. The testing was continued to almost 60 cycles, with no evidence of corrosion observed with SAM2X5 and other amorphous-metal formulations of interest.

IV. DISCUSSION

It has been recognized that the corrosion resistance of both iron- and nickel based crystalline alloys can be enhanced through the additions of Cr, Mo and W for many years.[32-33] These alloying elements also enhanced the corrosion resistance of iron-based amorphous metals. While the pitting resistance equivalence number (PREN) was developed for crystalline alloys, it was

effectively used as a general guidance in determining maximum beneficial elemental concentrations of Cr, Mo and W used in the materials studied here [34-39]. One possible equation used for estimating the PREN for crystalline nickel-based alloys is [40]:

$$PREN = [\%Cr] + 1.5 \times ([\%Mo] + [\%W] + [\%Nb]) \quad (8)$$

Another equation used for estimating the PREN of austenitic and duplex stainless steels is [41]:

$$PREN = [\%Cr] + 3.3 \times ([\%Mo] + 0.5 \times [\%W]) + 16 \times [\%N] \quad (9)$$

PREN values for SAM1651, other amorphous alloys, and crystalline reference alloys were calculated using these formulae, assuming that the equation can be applied to an amorphous alloy, and are summarized in Table VIII. These calculations indicate that the resistance of the SAM1651 amorphous metal should be more resistant to localized corrosion than Type 316L stainless steel or Ni-based Alloy C-22. As in the case of crystalline Fe-based and Ni-based alloys, it was found experimentally that the addition of Cr, Mo, and W substantially increased the corrosion resistance of these amorphous alloys. The addition of Y is also believed to be beneficial. However, there was additional passive film stability, which cannot be attributed to composition alone, and may be attributable to the glassy structure. Additional work was required to further understand the relative roles of composition and crystalline structure in high-performance amorphous metal coatings, such as the ones discussed here.

V. CONCLUSIONS

SAM1651 has a low critical cooling rate (CCR), due to the addition of yttrium (Y), which enables it to be rendered as a completely amorphous thermal spray coating. The yttrium addition increases the viscosity of the alloy, thereby slowing the nucleation and growth kinetics of crystalline phases. Unfortunately, such increases in viscosity also make this material relatively difficult to gas atomize, with the powders having irregular shapes. Such non-spherical particle morphology causes pneumatic conveyance of the SAM1651 powder during thermal spray operations to be difficult. The production of nearly spherical gas-atomized SAM1651 powder with acceptable flow characteristics has required extensive particle sorting, exotic and expensive milling to eliminate irregularities, and significant process optimization.

The hypothesis that the corrosion resistance of Fe-based amorphous metals can be enhanced through application of heuristic principles related to the additions of chromium, molybdenum, tungsten and yttrium has been tested with SAM7 (SAM1651) and SAM8 formulations, and found to have merit. The decision to achieve enhanced corrosion resistance in these Fe-based amorphous metals was initially based upon two considerations. First, substantial enhancements in corrosion resistance had been observed in stainless steels and nickel based alloys by adding chromium, molybdenum, tungsten, as well as other alloying elements. Secondly, this enhancement in localized corrosion resistance can be quantified in the pitting resistance equivalence number, and could be used as a guide to determine the level of molybdenum addition necessary to achieve localized corrosion resistance comparable to nickel-based Alloy C-22, one of the benchmark materials. Electrochemical tests have been used to prove that corrosion performance comparable to nickel-based Alloy C-22 can be achieved with the new Fe-based amorphous metals in 5M CaCl2 at 105°C and seawater at 90°C.

Thermal spray coatings produced with early Fe-based amorphous metal formulations (SAM35, SAM40, and SAM40X3) had non-optimal elemental compositions, were produced with non-optimal thermal spray parameters (powder size, gun pressure, and particle velocity), and exhibited rusting after 13 cycles in the standardized salt fog tests. However, dense and pore-free thermal spray coatings produced with improved amorphous metal formulations that have greater concentrations of chromium, molybdenum and yttrium (SAM7, also known as SAM1651) showed no corrosion after more than 30 cycles (and up to 54 cycles) in the salt fog test. Such performance cannot be achieved with thermally sprayed Type 316L stainless steel, as this material loses most of its desirable corrosion-resistance during the thermal spray process. To a lesser extent, similar difficulties are encountered during the thermal spraying of Alloy C-22.

The second hypothesis tested was that amorphous metals can have better corrosion resistance than comparable, crystalline materials. Ingots and melt-spun ribbons of the Fe-based SAM7 (SAM1651) and SAM8 amorphous metals, both free of grain boundaries, have shown much more resistance to corrosion (passive film stability) in aggressive environments such as 5M $CaCl_2$ at 105°C than crystalline Type 316L stainless steel and nickel-based Alloy C-22. It has also been found that it is not been possible to render Alloy C-22 as thermal spray coating with the same corrosion resistance as the wrought alloy, though such possibilities do exist with some of the Fe-based amorphous metal formulations discussed here.

It has been shown that these novel ultra-hard corrosion-resistant materials can be produced as either bulk alloys or coatings. For example, melt spinning and arc melting with drop casting can be used to render these materials as fully dense pore-free bulk alloys. Coatings can be produced with advanced thermal spray processes, or by physical vapor deposition processes such as magnetron sputtering or electron-beam evaporation. The materials can also be rendered as bulk alloys by using HVOF to form large plates on a flat mandrel. Near theoretical density has been achieved through precise control of powder size with atomization and classification.

Given the good performance of thermal-spray coatings of SAM1651 in salt fog and seawater environments, these coatings should be able to protect a variety of ships and marine structures, including off-shore drilling platforms. The performance in hot calcium chloride may indicate that this material could be used in processes where hot geothermal brines are involved. Ultimately, it may be possible to use materials such as these to help protect the outer surface of containers for the transportation, aging, and disposal of spent nuclear fuel, and to protect welds and heat affected zones, thereby preventing exposure to environments that might cause stress corrosion cracking, and as a means of criticality control inside containers [XX]. In the future, it may be possible to substitute such high-performance iron-based materials for more-expensive nickel-based alloys, thereby enabling cost savings in a wide variety of industrial applications.

ACKNOWLEDGMENTS

This work was done under the auspices of the U.S. DOE by Lawrence Livermore National Laboratory (LLNL) under Contract No. W-7405-Eng-48. Work was sponsored by the United States Department of Energy (DOE), Office of Civilian and Radioactive Waste Management (OCRWM); and Defense Advanced Research Projects Agency (DARPA), Defense Science Office (DSO). The guidance of Leo Christodoulou at DARPA DSO and of Jeffrey Walker at DOE OCRWM is gratefully acknowledged.

REFERENCES

1. M. Telford: The case for bulk metallic glass. *Materials Today*, **3,** 36-43 (2004).
2. N. R. Sorensen and R. B. Diegle: Corrosion of amorphous metals. In *Corrosion, Metals Handbook*, 9th Ed., Vol. 13, edited by J. R. Davis and J. D. Destefani (American Society of Metals International, Metals Park, OH, 1987), pp. 864-870.
3. R. M. Latanison: Corrosion resistance of metastable alloys processed by rapid solidification. *Workshop on Amorphous Metals and Semiconductors*, May 12-18, 1985 (Electric Power Research Institute, 1985).
4. D. E. Polk and B. C. Giessen: Overview of principles and applications. Chapter 1, In *Metallic Glasses*, edited by J. J. Gilman and H. J. Leamy (American Society of Metals International, Metals Park, OH, 1978), pp. 2-35.
5. K. Kishitake, H. Era, and F. Otsubo: Characterization of plasma sprayed Fe-10Cr-10Mo-(C,B) amorphous coatings. *J. Thermal Spray Technology*, **5** (2), 145-153 (1996).
6. S. Pang, T. Zhang, K. Asami, and A. Inoue: Effects of chromium on the glass formation and corrosion behavior of bulk glassy Fe-Cr-Mo-C-B alloys. *Materials Transactions*, **43** (8), 2137-2142 (2002).
7. S. J. Pang, T. Zhang, K. Asami, and A. Inoue: Synthesis of Fe-Cr-Mo-C-B-P bulk metallic glasses with high corrosion resistance. *Acta Materialia*, **50**, 489-497 (2002).
8. D. J. Branagan, Method of modifying iron-based glasses to increase crystallization temperature without changing melting temperature. U.S. Patent Application No. 20040250929, Filed Dec. 16, 2004.
9. D. J. Branagan: Properties of amorphous/partially crystalline coatings. U.S. Patent Application No. 20040253381, Filed Dec. 16, 2004.
10. J. C. Farmer, J. J. Haslam, S. D. Day, T. Lian, R. Rebak, N. Yang, and L. Aprigliano: Corrosion resistance of iron-based amorphous metal coatings. Paper PVP2006-ICPVT11-93835, In *Pressure Vessels and Piping Division Conference, Vancouver, BC, July 23-27, 2006* (ASME, New York, NY, 2006a).
11. J. Farmer, J. Haslam, S. Day, T. Lian, C. Saw, P. Hailey, J-S. Choi, N. Yang, C. Blue, W. Peter, J. Payer and D. Branagan: Corrosion resistances of iron-based amorphous metals with yttrium and tungsten additions in hot calcium chloride brine and natural Seawater, $Fe_{48}Mo_{14}Cr_{15}Y_2C_{15}B_6$ and W-containing variants. In *Critical Factors in Localized Corrosion 5, A Symposiun in Honor of Hugh Issacs*, edited by N. Missert, Electrochemical Society Transations, Vol. 3, 210th Meeting of the ECS, Cancun, Mexico, 2006 (ECS, Pennington, NJ, 2006b).
12. J. Farmer, J. Haslam, S. Day, T. Lian, C. Saw, P. Hailey, J-S. Choi, R. Rebak, N. Yang, R. Bayles, L. Aprigliano, J. Payer, J. Perepezko, K. Hildal, E. Lavernia, L. Ajdelsztajn, D. J. Branagan, and M. B. Beardsely: A high-performance corrosion-resistant iron-based amorphous metal – the effects of composition, structure and environment on corrosion resistance. *Scientific Basis for Nuclear Waste Management XXX*, Symposium NN, Boston, MA, Nov. 27 – Dec. 1, 2006 (Materials Research Society, 2006).
13. T. Lian, D. Day, P. Hailey, J-S. Choi, and J. Farmer: Comparative study on the corrosion resistance of Fe-based amorphous metal, borated stainless steel and Ni-Cr-Mo-Gd alloy. Scientific Basis for Nuclear Waste Management XXX, Symposium NN, Boston, MA, Nov. 27 – Dec. 1, 2006 (Materials Research Society, 2006).

14. H. Shinimiya, A. Nakazawa, Z. Kato, A. A. El Moneium, Y. Niizeki, K. Asami, and K. Hashimoto: Corrosion resistant bulk amorphous Ni-Cr-Ta-Mo-Nb-5P alloys in concentrated hydrochloric acids. Paper 319, *Session on Corrosion and Electrochemistry of Advanced Materials in Honor of Koji Hashimoto*, 208th Meeting of the Electrochemical Society, Westing Bonaventure Hotel, Los Angeles, California, October 16-21, 2005 (Electrochemical Society, Pennington, NJ, 2005).
15. D. Chidambaram, C. R. Clayton, and M. R. Dorfman: Evaluation of the electrochemical behavior of HVOF-sprayed alloy coatings. *Surface and Coatings Technology*, **176**, 307-317 (2004).
16. F. Guo, S. J. Poon, and G. J. Shiflet: Metallic glass ingots based on yttrium. *Metallic Applied Physics Letters*, **83** (13), 2575-2577 (2003).
17. Z. P. Lu, C. T. Liu, and W. D. Porter: Role of yttrium in glass formation of Fe-based bulk metallic glasses. *Metallic Applied Physics Letters*, **83** (13), 2581-2583 (2003).
18. V. Ponnambalam, S. J. Poon, and G. Shiflet: *J. Materials Research*, **19** (5), 1320, 2004.
19. J. C. Farmer, J. J. Haslam, S. D. Day, D. J. Branagan, C. A. Blue, J. D. K. Rivard, L. F. Aprigliano, N. Yang, J. H. Perepezko, and M. B. Beardsley: Paper PVP2005-71664, Pressure Vessels and Piping Division Conference, Denver, CO, July 17-21, 2005 (American Society of Mechanical Engineers, Three Park Avenue, New York, NY, 2005).
20. J. C. Farmer, J. J. Haslam, S. D. Day, T. Lian, R. Rebak, N. Yang, and L. Aprigliano: Corrosion resistance of iron-based amorphous metal coatings. Paper PVP2006-ICPVT11-93835, *Pressure Vessels and Piping Division Conference*, Vancouver, BC, July 23-27, 2006 (American Society of Mechanical Engineers, Three Park Avenue, New York, NY, 2006).
21. J. Farmer, S. Lu, D. McCright, G. Gdowski, F. Wang, T. Summers, P. Bedrossian, J. Horn, T. Lian, J. Estill, A. Lingenfelter, and W. Halsey: General and localized corrosion of high-level waste container in Yucca Mountain. Pressure Vessel and Piping Conference, Seattle, WA, July 23-27, 2000, In *Transportation, Storage, and Disposal of Radioactive Materials*, PVP Vol. 408 (American Society of Mechanical Engineers, Three Park Avenue, New York, NY, 2000), pp. 53-70.
22. J. R. Scully, J. L. Hudson, T. Lunt, G. Ilevbare, and B. Kehler: Localized corrosion initiation and transition to stabilization in alloys 625 and C-22. Final Report, TRW/DOE Yucca Mountain Project Purchase Order No. A10762JM8A (University of Virginia, Charlottesville, VA, Sep. 30, 1999).
23. K. A. Gruss, G. A. Cragnolino, D. S. Dunn, and N. Sridar: Repassivation potential for localized corrosion of alloys 625 and C22 in simulated repository environments. Paper 149, Corrosion 98 (National Association of Corrosion Engineers, Houston, TX, 1998).
24. C. K. Saw: In *X-ray Scattering Techniques for Characterization Tools in the Life Sciences, Nanotechnologies for the Life Science*, edited by Challa Kumar (Wiley-VCH Verlag GmbH and Company, KGaA, Weinheim, 2006).
25. C. K. Saw and R. B. Schwarz: Chemical short-range order in dense random-packed models. *J. Less-Common Metals*, **140**, 385-393 (1988).
26. Standard reference test method for making potentiostatic and potentiodynamic anodic polarization measurements. Designation G 5-94, In *1997 Annual Book of American Society for Testing and Materials Standards,* Section 3, Vol. 3.02 (American Society for Testing and Materials, 1997), pp. 54–57.
27. Standard reference test method for making potentiostatic and potentiodynamic anodic polarization measurements. Designation G 5-87, In *1989 Annual Book of American Society*

for Testing and Materials Standards, Section 3, Vol. 3.02 (American Society for Testing and Materials, 1989), pp. 79–85.
28. Standard practice for conventions applicable to electrochemical measurements in corrosion testing. Designation G 3-89, In *1997 Annual Book of American Society for Testing and Materials Standards*, Section 3, Vol. 3.02, (American Society for Testing and Materials, 1997), pp. 36–44.
29. Standard test method for conducting cyclic potentiodynamic polarization measurements for localized corrosion susceptibility of iron-, nickel-, or cobalt-based alloys. Designation G 61-86, In 1997 Annual Book of American Society for Testing and Materials Standards, Section 3, Vol. 3.02 (American Society for Testing and Materials, 1997), pp. 231–235.
30. R. S. Treseder, R. Baboian, and C. G. Munger: Polarization resistance method for determining corrosion rates. In *Corrosion Engineer's Reference Book*, 2nd Ed. (National Association of Corrosion Engineers, Houston, TX, 1991), pp. 65-66.
31. D. A. Jones: Electrochemical kinetics of corrosion – Faraday's law. In *Principles and Prevention of Corrosion*, 2nd Ed., Chapter 3, Section 3.1.1, Equations 3-5 (Prentice Hall, Upper Saddle River, NJ, 1996), pp. 75–76.
32. A. J. Bard and L. R. Faulkner: Potentials and thermodynamics of cells – liquid junction potentials. In *Electrochemical Methods, Fundamentals and Applications*, Chapter 2, Section 2.3, Table 2.3.2, Equation 2.3.39 (John Wiley and Sons, New York, NY, 1980), p. 67, 71.
33. H. P. Hack: Crevice corrosion behavior of molybdenum-containing stainless steel in seawater. *Materials Performance*, **22** (6) 24–30 (1983).
34. A. I. Asphahani: Corrosion resistance of high performance alloys. *Materials Performance*, **19** (12) 33–43 (1980).
35. J. C. Farmer et al.: High-performance corrosion-resistant amorphous metals. *Global 2003*, New Orleans, LA, 2003 (American Nuclear Society, 2003).
36. D. J. Branagan, M. C. Marshall, and B. E. Meacham: High performance corrosion resistant materials for naval warfighting and safe long-term storage/disposal of spent nuclear fuel. *Final Report*, LLNL Subcontract, LLNL-RFP-B550033 (Institute of Nanomaterials Research and Development, The NanoSteel Company, Idaho Falls, ID, 2005) 84 pages.
37. J. Farmer, C. Earl, C. Doty, D. Spence, J. Walker, F. Wong, J. Payer, G-Q. Lu, D. E. Clark, D. C. Folz, A. Heuer, O. Graeve, D. Branagan, C. Blue, J. Rivard, J. Perepezko, L. Kaufman, N. Yang, E. Lavernia, J. Haslam, E. Lemieux, L. Aprigliano, B. Beardsley, T. Weaver, B. Edwards, B. Brown, A. Halter, B Bayles and J. Lewandowski: *DARPA-DOE High Performance Corrosion-Resistant Materials Principal Investigator's Meeting*, Turtle Bay Resort, Oahu, Hawaii, January 10-13, 2005, UCRL-PRES-214672 (Lawrence Livermore National Laboratory, Livermore, CA, 2005), 407 pages.
38. J. C. Farmer, J. J. Haslam and S. D. Day: High-performance corrosion-resistant iron-based amorphous-metal coatings – evaluation of corrosion resistance. *HPCRM Annual Report*, UCRL-SR-218144 (Lawrence Livermore National Laboratory, Livermore, CA, 2006), 68 pages.
39. J. C. Farmer, J-S. Choi, J. J. Haslam, S. D. Day, N. Yang, T. Headley, G. Lucadamo, J. L Yio, J. Chames, A. Gardea, M. Clift, C. A. Blue, W. H. Peters, J. D. K. Rivard, D. C. Harper, D. Swank, R. Bayles & E. J. Lemieux, Robert Brown & Theresa M. Wolejsza, L. F. Aprigliano, D. J. Branagan, M. C. Marshall, Brian E. Meacham, E. Joseph Buffa, M. Brad Beardsley, E. J. Lavernia, J. Schoenung, L. Ajdelsztajn, J. Dannenberg, O. A. Graeve, J. J. Lewandowski, John H. Perepezko, Kjetil Hildal, L. P. Kaufman, J. Boudreau: High-

performance corrosion-resistant iron-based amorphous metal coatings. *Team FY05 HPCRM Annual Report*, UCRL-SR-219257 (Lawrence Livermore National Laboratory, Livermore, CA, 2006), 138 pages.

40. J. Farmer, J. Haslam, S. Day, T. Lian, C. Saw, P. Hailey, J-S. Choi, N. Yang, C. Blue, W. Peter, R. Bayles, R. Brown, J. Payer, J. Perepezko, K. Hildal, E. Lavernia, L. Ajdelsztajn, D. J. Branagan, J. Buffa, M. Beardsley, L. Aprigliano and J. Boudreau: Corrosion resistance of iron-based amorphous metals in hot concentrated calcium chloride and seawater: $Fe_{48}Mo_{714}Cr_{15}Y_2C_{15}B_6$. UCRL-TM-224159 (Lawrence Livermore National Laboratory, Livermore, CA, Aug. 30, 2006), 47 pages.
41. C. Thornton and C. Cooper: Overmatching superalloy consumable Inco-weld, 686CPT broadens its applications to include welding super austenitic and super duplex stainless steels, In *Stainless Steel World* (KCI Publishing BV 1, 2004).
42. Pitting corrosion. (www.corrosion-doctors.org/localized/pitting.htm, Dec. 23, 2006).

TABLES

Table I – Fe-based SAM40 composition, with 1, 3, 5, and 7 atomic percent additions of specific elements believed to be beneficial to glass formation or corrosion resistance. Elemental additions investigated included nickel (Ni), molybdenum (Mo), yttrium (Y), titanium (Ti), zirconium (Zr) and chromium (Cr). The two formulations of greatest interest at the present time, based upon corrosion resistance and ease of processing are SAM2X5 ($Fe_{49.7}Cr_{17.7}Mn_{1.9}Mo_{7.4}W_{1.6}B_{15.2}C_{3.8}Si_{2.4}$), which has a relatively high CCR, and yttrium-containing SAM1651 or SAM7 ($Fe_{48.0}Cr_{15.0}Mo_{14.0}B_{6.0}C_{15.0}Y_{2.0}$), which has a relatively low CCR.

Nominal or Target Composition Used to Prepare Samples in Atomic Percent														
Alloy	Specification / Formula	Fe	Cr	Mn	Mo	W	B*	C*	Si	Y	Ni	P*	Co	Total
316L	UNS S31603	68.0	18.0	1.5	1.5	0.0	0.0	0.0	1.0	0.0	10.0	0.0	0.0	100
C-22	UNS N06022	4.0	25.0	0.1	8.0	1.4	0.0	0.0	1.0	0.0	60.0	0.0	0.5	100
SAM40	$Fe_{52.3}Mn_2Cr_{19}Mo_{2.5}W_{1.7}B_{16}C_4Si_{2.5}$	52.3	19.0	2.0	2.5	1.7	16.0	4.0	2.5	0.0	0.0	0.0	0.0	100
SAM3X1	$(SAM40)_{99} + Y_1$	51.8	18.8	2.0	2.5	1.7	15.8	4.0	2.5	1.0	0.0	0.0	0.0	100
SAM3X3	$(SAM40)_{97} + Y_3$	50.7	18.4	1.9	2.4	1.6	15.5	3.9	2.4	3.0	0.0	0.0	0.0	100
SAM3X5	$(SAM40)_{95} + Y_5$	49.7	18.1	1.9	2.4	1.6	15.2	3.8	2.4	5.0	0.0	0.0	0.0	100
SAM3X7	$(SAM40)_{93} + Y_7$	48.6	17.7	1.9	2.3	1.6	14.9	3.7	2.3	7.0	0.0	0.0	0.0	100
SAM1651	$Fe_{48}Mo_{14}Cr_{15}Y_2C_{15}B_6$	48.0	15.0	0.0	14.0	0.0	6.0	15.0	0.0	2.0	0.0	0.0	0.0	100

Table II – The conversion of the corrosion current density to penetration rate (corrosion rate) requires the parameters summarized in this table. These penetration rates are for an assumed current density of one microamp per square centimeter (1 μA cm^{-2}). If the corrosion rate is 2 μA cm^{-2} instead of the assumed 1 μA cm^{-2}, the penetration rate is simply doubled. The value of Faraday's constant (F) is 96,484.6 C $equiv^{-1}$.

Alloy	ρ_{alloy}	$n_{alloy} = (f_j n_j / a_j)/100$		$(dp/dt) = (i_{corr})/(\rho_{alloy} \times n_{alloy} \times F)$			
	g cm^{-3}			cm sec^{-1}		μm $year^{-1}$	
		Low	High	Low	High	Low	High
Type 316L	7.85	3.90×10^{-2}	6.53×10^{-2}	2.02×10^{-11}	3.38×10^{-11}	6.38	10.7
Alloy C-22	8.69	3.80×10^{-2}	6.75×10^{-2}	1.77×10^{-11}	3.14×10^{-11}	5.57	9.89
SAM2X5	7.65	5.41×10^{-2}	7.93×10^{-2}	1.71×10^{-11}	2.50×10^{-11}	5.39	7.89
SAM1651	7.70	4.70×10^{-2}	8.02×10^{-2}	1.68×10^{-11}	2.87×10^{-11}	5.29	9.04

Table III – A description of the standard GM9540P Salt Fog Test is summarized here. Note that the salt solution mists (denoted with asterisks) consisted of 1.25% solution containing 0.9% sodium chloride, 0.1% calcium chloride, and 0.25% sodium bicarbonate.

24-Hour Test Cycle for GM9540P Accelerated Corrosion Test		
Shift	Elapsed Time (hrs)	Event
Ambient Soak	0	Salt solution mist for 30 seconds, followed by ambient exposure at 13-28°C (55-82°F)
	1.5	Salt solution mist for 30 seconds, followed by ambient exposure at 13-28°C (55-82°F)
	3	Salt solution mist for 30 seconds, followed by ambient exposure at 13-28°C (55-82°F)
	4.5	Salt solution mist for 30 seconds, followed by ambient exposure at 13-28°C (55-82°F)
Wet Soak	8 to 16	High humidity exposure for 8 hours at 49 ± 0.5°C (120 ± 1°F) and 100% RH, including a 55-minute ramp to wet conditions
Dry Soak	16 to 24	Elevated dry exposure for 8 hours at 60 ± 0.5°C (140 ± 1°F) and less than 30% RH, including a 175-minute ramp to dry conditions

Table IV – The actual compositions of several samples used in this study were determined with energy dispersive X-ray spectroscopy (EDS), and are summarized here. The measurements were done for wrought samples of Type 316L stainless steel and nickel-based Alloy C-22; melt-spun ribbons of SAM40, SAM2X1, SAM2X3, SAM2X5 and SAM2X7; and a drop-cast SAM1651 ingot. Attempts to produce melt spur ribbons of SAM7 resulted in a final composition of only 0.2 atomic percent yttrium.

Actual Compositions Determined by Energy Dispersive X-Ray Spectroscopy in Atomic Percent														
Alloy	Specification / Formula	Fe	Cr	Mn	Mo	W	B*	C*	Si	Y	Ni	P*	Co	Total
Type 316L	UNS S31603	67.6	18.7	1.3	1.2	0.0	0.0	0.0	1.2	0.0	10.0	0.0	0.0	100
Alloy C-22	UNS N06022	3.9	25.2	0.1	7.8	1.4	0.0	0.0	1.1	0.0	60.0	0.0	0.5	100
SAM40	$Fe_{52.3}Mn_2Cr_{19}Mo_{2.5}W_{1.7}B_{16}C_4Si_{2.5}$	51.9	19.2	2.6	2.5	1.5	16.0	4.0	2.2	0.0	0.0	0.0	0.0	100
SAM3X1	$(SAM40)_{99} + Y_1$	49.1	19.2	1.8	3.1	3.0	15.8	4.0	2.9	1.0	0.0	0.0	0.0	100
SAM3X3	$(SAM40)_{97} + Y_3$	49.4	18.9	1.7	3.0	2.8	15.5	3.9	1.9	2.9	0.0	0.0	0.0	100
SAM3X5	$(SAM40)_{95} + Y_5$	48.8	18.4	1.5	2.6	2.6	15.2	3.8	2.2	4.8	0.0	0.0	0.0	100
SAM3X7	$(SAM40)_{93} + Y_7$	47.3	17.8	2.1	2.5	2.6	14.9	3.7	2.2	6.8	0.0	0.0	0.0	100
SAM1651	$Fe_{48}Mo_{14}Cr_{15}Y_2C_{15}B_6$	49.1	14.6	0.0	13.9	0.0	5.9	14.0	0.3	1.9	0.2	0.0	0.0	100

Table V – Thermal analysis data (DTA or DSC) for Fe-based glass forming alloys suitable for thermal spray deposition as summarized in this table. The two formulations of greatest interest at the present time are SAM2X5 ($Fe_{49.7}Cr_{17.7}Mn_{1.9}Mo_{7.4}W_{1.6}B_{15.2}C_{3.8}Si_{2.4}$), which has a relatively high CCR, and yttrium-containing SAM1651 or SAM7 ($Fe_{48.0}Cr_{15.0}Mo_{14.0}B_{6.0}C_{15.0}Y_{2.0}$), which has a relatively low CCR. These selections are based upon their good corrosion resistance and relative ease or processing.

Alloy	T_g (°C)	T_x (°C)	T_m (°C)	T_L (°C)	T_{rg}
SAM40	568-574	623	1110	1338	0.53
SAM3X1	560	614	1108	min. 1320	0.52
SAM3X3	573	659	1138	min. 1380	0.51
SAM3X5	590	677	1143	min. 1400	0.52
SAM3X7	Not resolved	697	1164	min. 1420	Not resolved
SAM1651	584	653	1121	1290	0.55

Table VI – The hardness (kg mm^{-2}) for as-sprayed SAM1651 HVOF coatings is summarized here.

HV100									
Indentation	HV1	HV2	HV3	HV4	HV5	HV6	HV7	HV8	HV9
1	1046	1191	840	1232	1097	955	1048	1183	931
2	1129	1103	1181	1175	1121	988	1202	1140	903
3	1004	1022	978	1130	979	1089	1155	1035	827
4	861	1059	1104	1033	1120	1075	1160	1105	893
5	883	1115	1154	1075	1043	975	1205	1058	979
Average	985	1098	1051	1129	1072	1016	1154	1104	907
Std. Dev.	112	64	142	79	61	61	64	60	56
HV300									
Indentation	HV1	HV2	HV3	HV4	HV5	HV1	HV2	HV3	HV4
1	919	994	910	985	894	987	992	908	856
2	789	1038	889	861	876	870	1058	1024	908
3	784	1005	848	848	887	944	965	1050	921
4	892	1004	1011	977	886	837	970	911	880
5	901	943	854	810	917	876	971	924	894
Average	857	997	902	896	892	903	991	963	892
Std. Dev.	65	34	66	80	15	61	39	68	25

Table VII – Values of the polarization resistance, corrosion current density, and corrosion rate, measured with linear polarization, measured in natural seawater at 30°C, are summarized for HVOF coatings of SAM1651 and Alloy C-22, as well as wrought samples of Alloy C-22. Values of the open circuit corrosion potential are also presented.

Natural Seawater at 30°C						
Sample ID	Material	Value	E_{corr}	R_p	I_{corr}	Corrosion Rate
			mV	ohms cm²	μA/cm²	(μm/yr)
E316L443	HVOF SAM2X5	Average	-87	1.63×10^{6}	2.72×10^{-2}	0.1789
		Std. Dev.	6	1.37×10^{6}	1.36×10^{-2}	0.1071
E316L407	HVOF SAM1651	Average	-73	8.35×10^{5}	3.56×10^{-2}	0.3214
		Std. Dev.	4	4.67×10^{5}	1.51×10^{-2}	0.1368
JE1589 C22	Wrought Alloy C-22	Average	-163	2.74×10^{6}	9.12×10^{-3}	0.0972
		Std. Dev.	1	9.13×10^{4}	3.02×10^{-4}	0.0032
CC-22 4000	Wrought Alloy C-22	Average	-312	6.23×10^{7}	5.07×10^{-3}	0.0501
		Std. Dev.	3	1.02×10^{8}	4.40×10^{-3}	0.0435

Table VIII – Values of the polarization resistance, corrosion current density, and corrosion rate, measured with linear polarization, measured in natural seawater at 90°C, are summarized for HVOF coatings of SAM1651 and Alloy C-22, as well as wrought samples of Alloy C-22. Values of the open circuit corrosion potential are also presented.

Natural Seawater at 90°C						
Sample ID	Material	Value	E_{corr}	R_p	I_{corr}	Corrosion Rate
			mV	ohms cm²	μA/cm²	(μm/yr)
E316L442	HVOF SAM2X5	Average	-241	1.25×10^{5}	2.00×10^{-1}	1.580
		Std. Dev.	7	1.04×10^{4}	1.73×10^{-2}	0.137
E316L402	HVOF SAM1651	Average	-228	1.76×10^{5}	1.42×10^{-1}	1.284
		Std. Dev.	3	6.15×10^{3}	5.05×10^{-3}	0.046
JE1594 C22	Wrought Alloy C-22	Average	-319	7.69×10^{4}	3.25×10^{-1}	3.216
		Std. Dev.	1	4.95×10^{2}	2.10×10^{-3}	0.021
CC-22 4002 #1	Wrought Alloy C-22	Average	-340	7.73×10^{4}	3.24×10^{-1}	3.199
		Std. Dev.	0	1.03×10^{3}	4.29×10^{-3}	0.042
CC-22 4002 #2	Wrought Alloy C-22	Average	-318	2.03×10^{5}	1.23×10^{-1}	1.216
		Std. Dev.	1	9.07×10^{2}	5.50×10^{-4}	0.005

Table IX – Values of the polarization resistance, corrosion current density, and corrosion rate, measured with linear polarization, measured in 5M $CaCl_2$ at 105°C, are summarized for HVOF coatings of SAM1651 and Alloy C-22, as well as wrought samples of Alloy C-22. Values of the open circuit corrosion potential are also presented.

5M $CaCl_2$ at 105°C						
Sample ID	Material	Value	E_{corr}	R_p	I_{corr}	Corrosion Rate
			mV	ohms cm²	μA/cm²	(μm/yr)
E316L456	HVOF SAM2X5	Average	-241	7.32×10^{4}	3.42×10^{-1}	2.696
		Std. Dev.	2	1.03×10^{3}	4.76×10^{-3}	0.038
E316L478	HVOF SAM1651	Average	-293	2.81×10^{4}	8.91×10^{-1}	8.048
		Std. Dev.	5	2.49×10^{2}	7.92×10^{-3}	0.072
E316L235	HVOF Alloy C-22	Average	-348	2.14×10^{3}	1.17×10^{1}	115.692
		Std. Dev.	5	8.94×10^{1}	4.82×10^{-1}	4.770
CC-22 4009	Wrought Alloy C-22	Average	-464	4.93×10^{4}	5.10×10^{-1}	5.040
		Std. Dev.	3	4.14×10^{3}	4.37×10^{-2}	0.433

Table X – Values of the pitting resistance equivalence number (PREN) for reference alloys and Fe-based amorphous metals.

Alloy	Low	Average	High
316L	23	26	30
C-22	43	46	50
SAM2X5	66	74	90
SAM1651	96	100	103

FIGURES

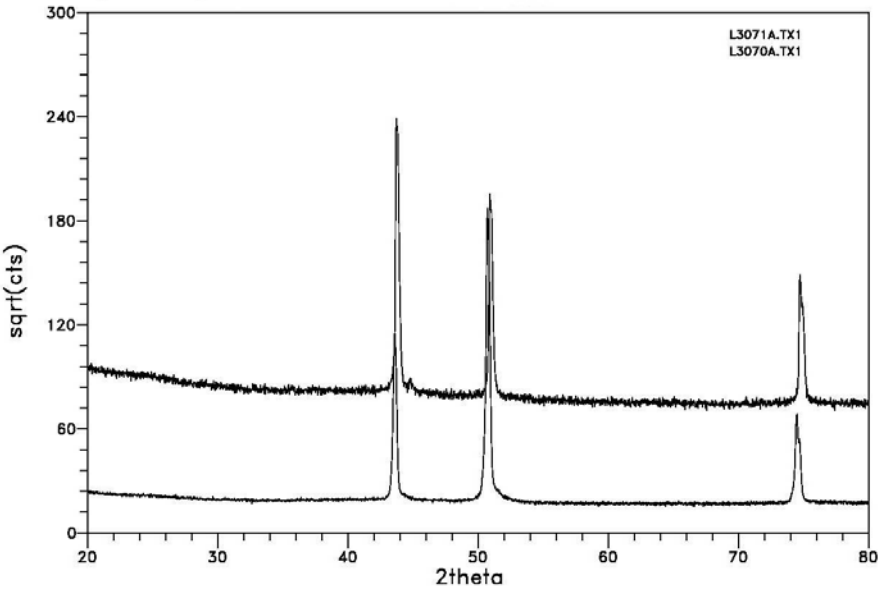

Figure 1 – This figure shows X-ray diffraction data for melt-spun ribbon (MSR) samples of Type 316L stainless steel and nickel-based Alloy C-22. The strong peaks are indicative of the crystalline nature of these materials.

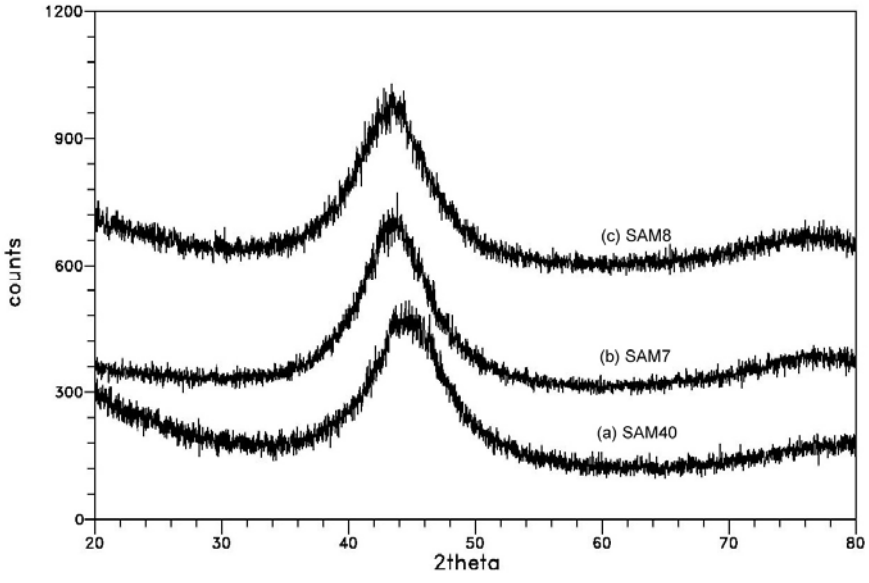

(b)

Figure 2 – This figure shows X-ray diffraction data for melt-spun ribbon (MSR) samples of iron-based amorphous metals identified as: (a) SAM40; (b) SAM7, which is also known as SAM1651; and (c) SAM8. These MSR samples are completely amorphous.

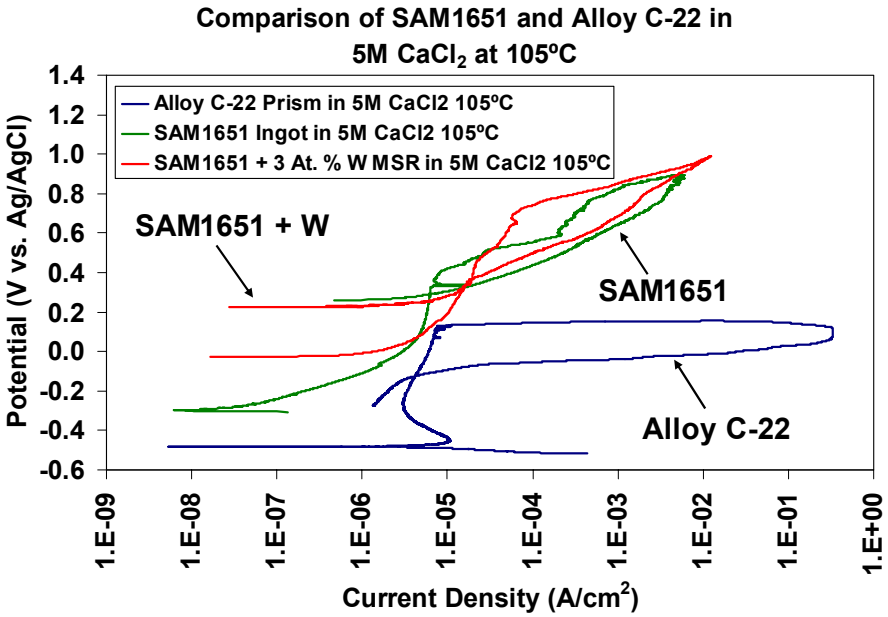

Figure 3 – Cyclic polarization data for a wrought prism of nickel-based Alloy C-22, a drop-cast ingot of iron-based SAM7 (SAM1651) amorphous metal, and a melt-spun ribbon of SAM8 (SAM1651 + 3 atomic percent tungsten), all obtained with 5M $CaCl_2$ at 105°C. Both the SAM7 and SAM8 showed passive film stability comparable to (or better than) Alloy C-22. The addition of 3 atomic-percent tungsten to the SAM1651 enhanced the passive film stability, and also yielded more ductile and damage-tolerant amorphous metal ribbons.

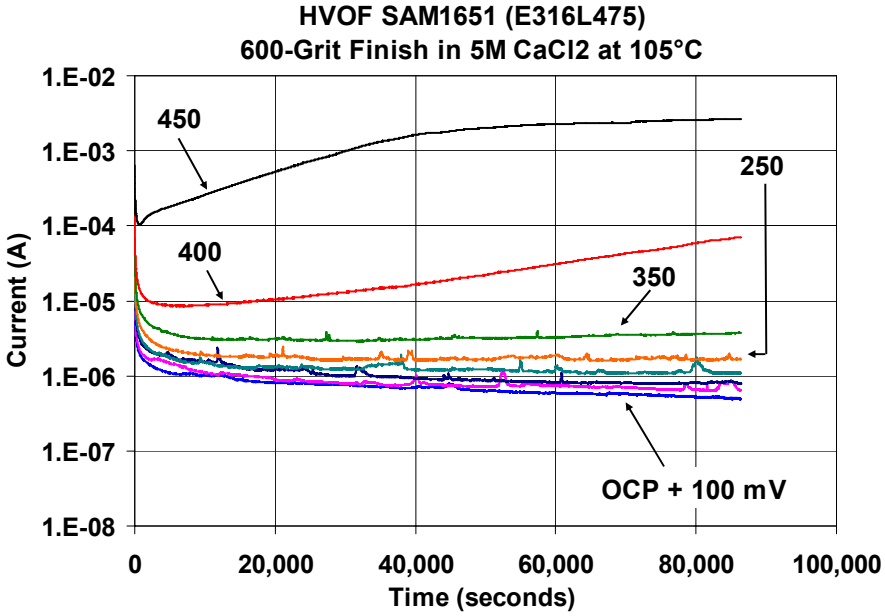

Figure 4 – Current transients wee measured at various levels of constant applied potential (100 to 450 mV vs. OCP) in 5M $CaCl_2$ at 105°C, for a polished SAM1651 HVOF coating on a Type 316L stainless steel (serial number E316L475).

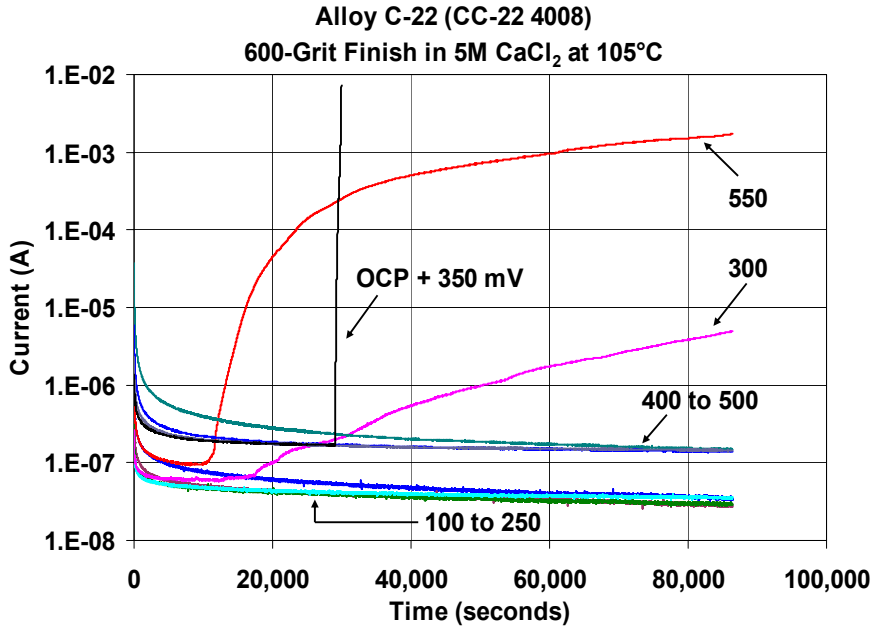

Figure 5 – Current transients were measured at various levels of constant applied potential ranging (100 to 550 mV vs. OCP) in 5M $CaCl_2$ at 105°C, for wrought Alloy C-22 (serial number CC-22 4008).

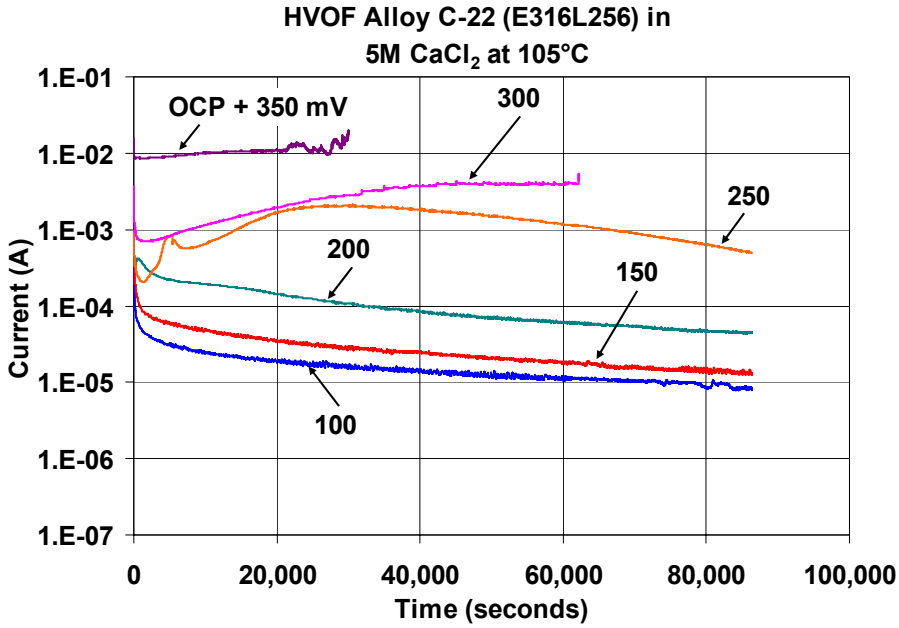

Figure 6 – Current transients were measured at various levels of constant applied potential (100 to 350 mV vs. OCP) in 5M $CaCl_2$ at 105°C, for an as-sprayed (unpolished) Alloy C-22 HVOF coating on Type 316L stainless steel (serial number E316L256).

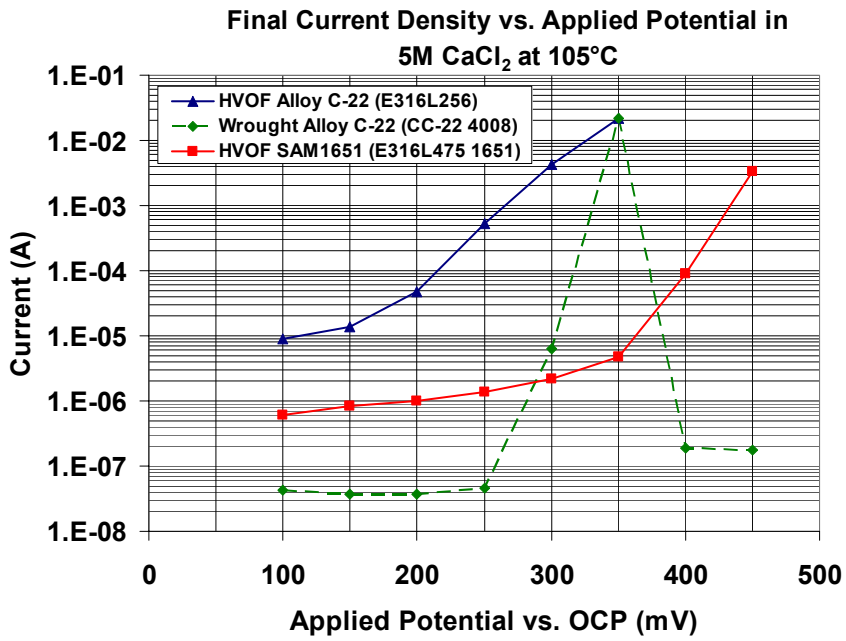

Figure 7 – Potential-step testing has been performed on HVOF coatings of SAM1651 and Alloy C-22 on Type 316L stainless steel, and wrought C-22, all in extremely aggressive 5M CaCl2 heated to 105°C. To eliminate the need for surface roughness corrections in the conversion of measured current and electrode area to current density, the SAM1651 coating was polished to a 600-grit finish prior to testing.

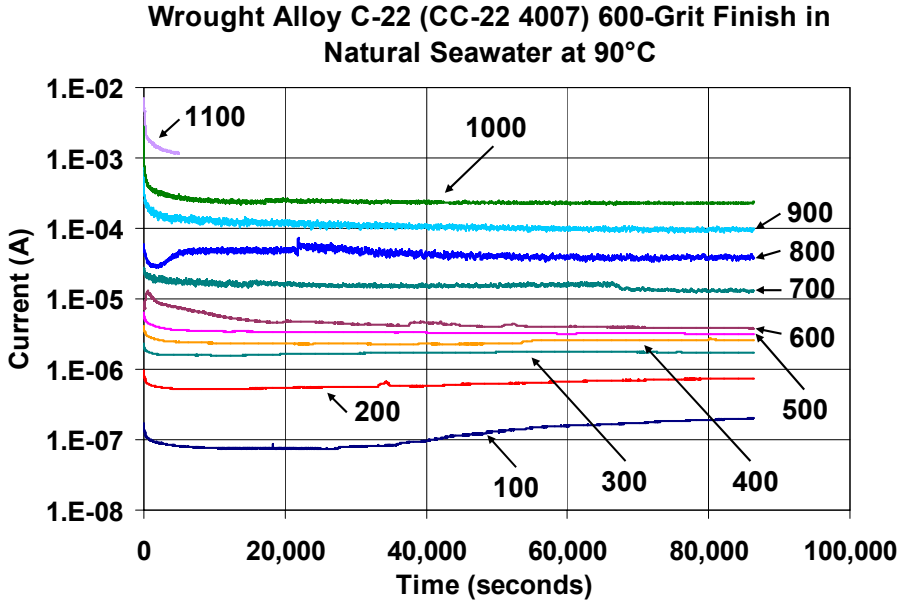

Figure 8 – Current transients at various levels of constant applied potential ranging from (100 to 1000 mV vs. OCP) in deaerated seawater at 90°C, for wrought nickel-based Alloy C-22 (serial number CC-22 4007).

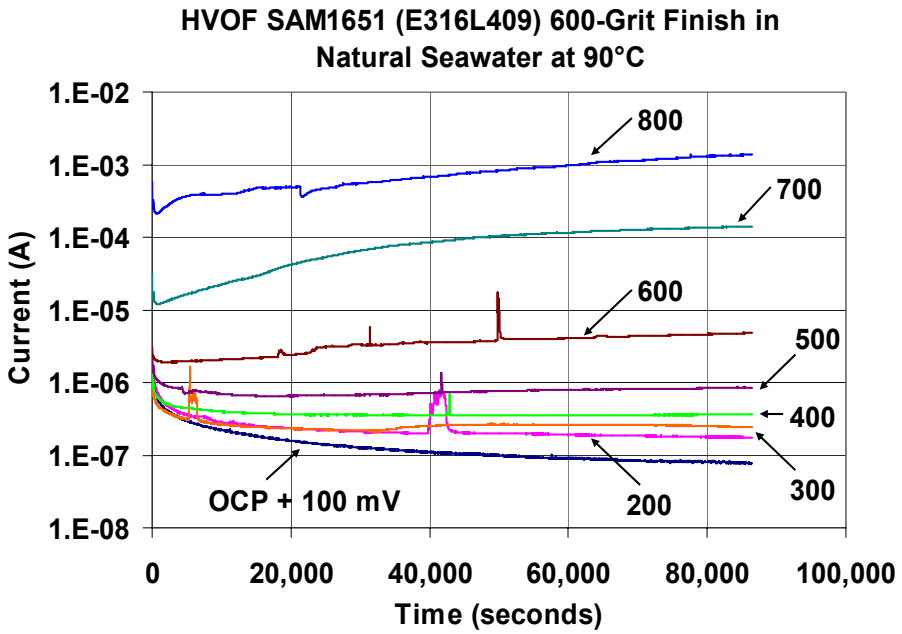

Figure 9 – Current transients were measured at various levels of constant applied potential (100 to 800 mV vs. OCP) in seawater at 90°C for a 600-grit polished SAM1651 HVOF coating on Type 316L stainless steel (serial number E316L409).

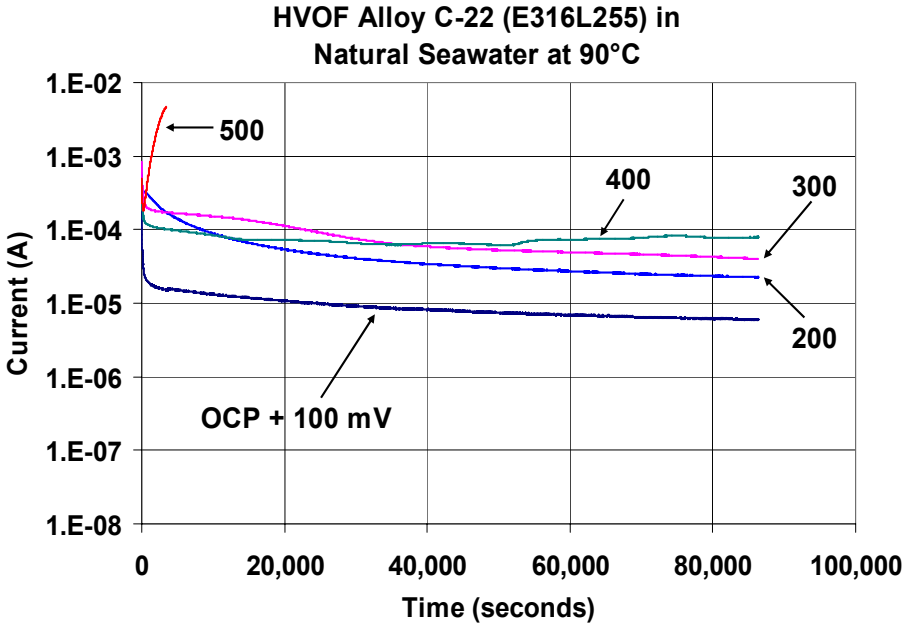

Figure 10 – Current transients were measured at various levels of constant applied potential (100 to 500 mV vs. OCP) in seawater at 90°C, for an as-sprayed (unpolished) Alloy C-22 HVOF coating on Type 316L stainless steel (serial number E316L255).

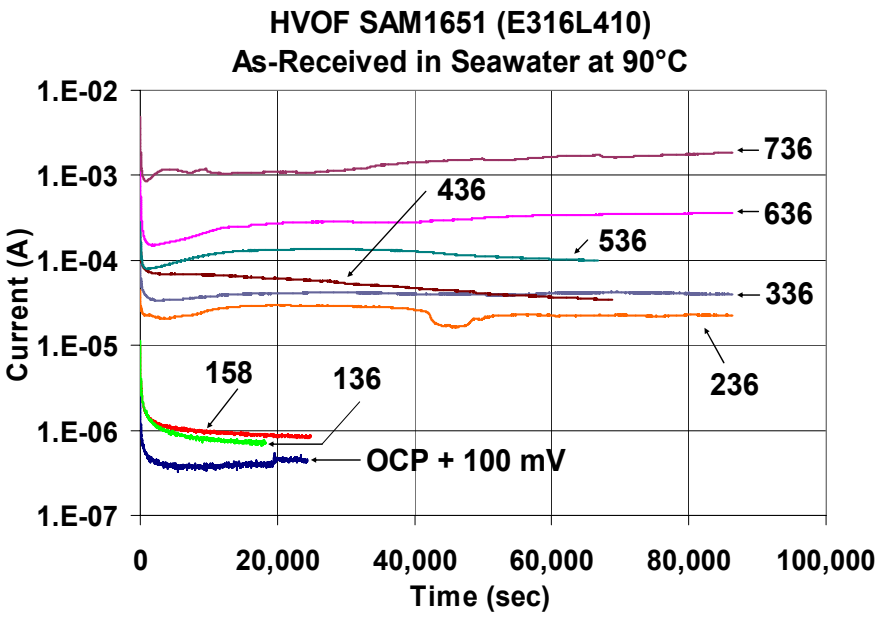

Figure 11 – Current transients were measured at various levels of constant applied potential (100 to 736 mV vs. OCP) in seawater at 90°C, for an as-sprayed (unpolished) HVOF coating of SAM1651 on a Type 316L stainless steel (serial number E316L410).

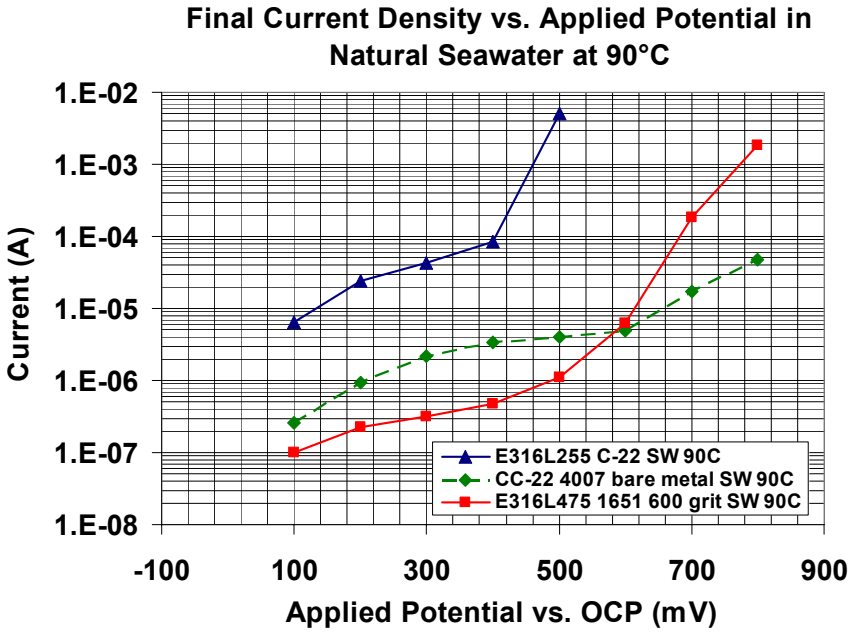

Figure 12 – Potential-step testing has been performed on HVOF coatings of SAM1651 and Alloy C-22 on Type 316L stainless steel, and wrought C-22, all in natural seawater heated to 90°C. To eliminate the need for surface roughness corrections in the conversion of measured current and electrode area to current density, the SAM1651 coating was polished to a 600-grit finish prior to testing.

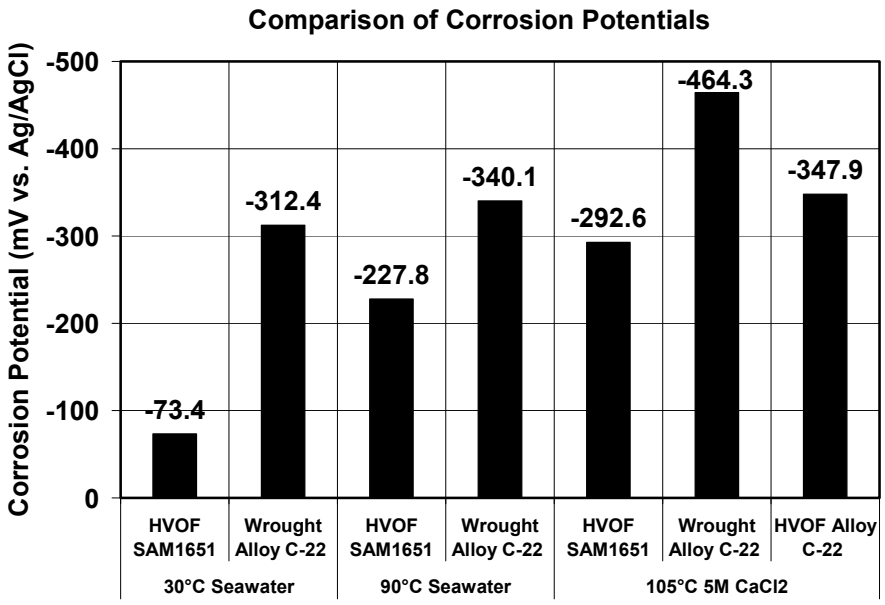

Figure 13 – The corrosion potentials for the thermal spray coatings of SAM1651 and the reference material (wrought nickel-based Alloy C-22) in three relevant environments, Half Moon Bay seawater at two temperature levels, and in hot concentrated calcium chloride (5M $CaCl_2$ at 105°C) are summarized.

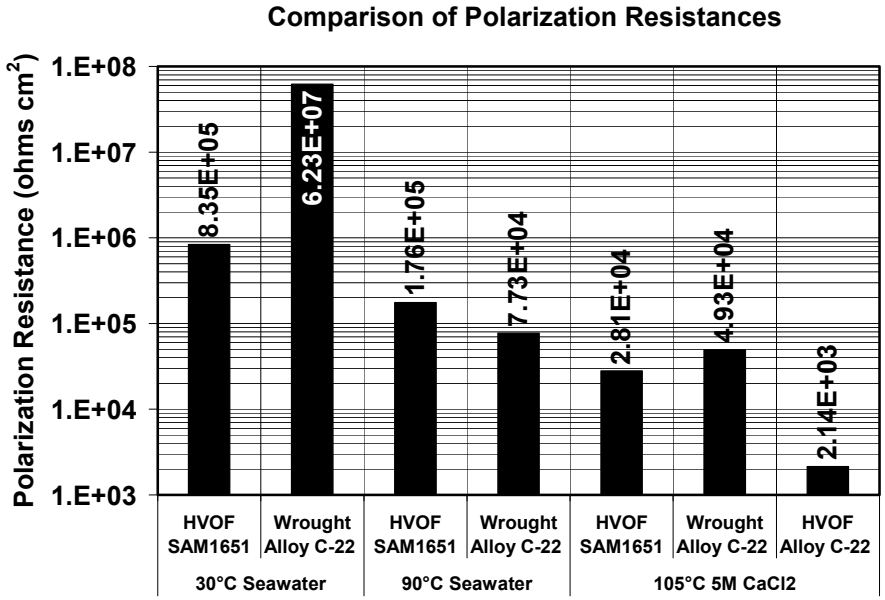

Figure 14 – Linear polarization was used to determine the polarization resistance for thermal spray coatings of SAM1651 and the reference material (wrought nickel-based Alloy C-22) in three relevant environments, Half Moon Bay seawater at two temperature levels, and in hot concentrated calcium chloride (5M $CaCl_2$ at 105°C).

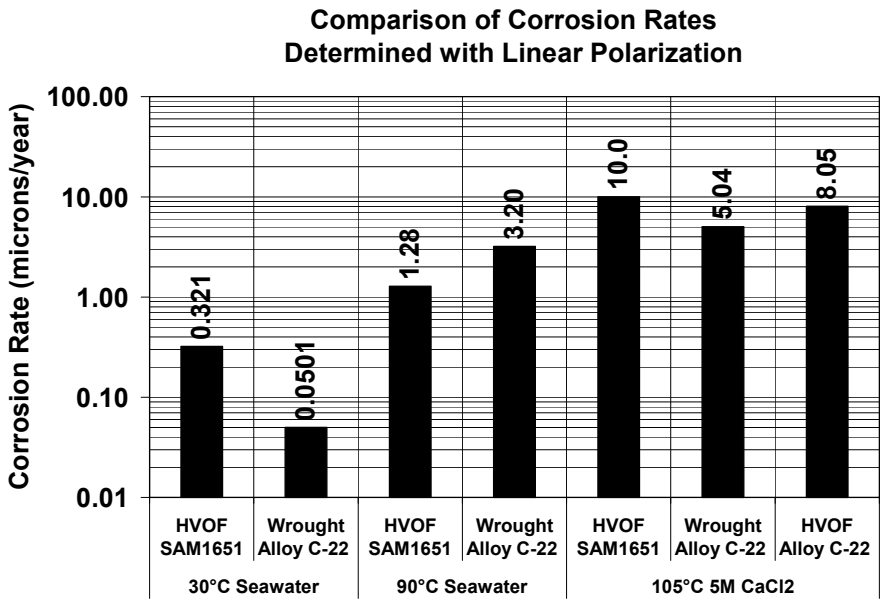

Figure 15 – Values of the polarization resistance shown in Figure 15 were converted to corrosion rates for the thermal spray coatings of SAM1651 and the reference material (wrought nickel-based Alloy C-22) in three relevant environments, natural seawater at two temperature levels, and in hot concentrated calcium chloride (5M $CaCl_2$ at 105°C).

Figure 16 – Salt fog testing was conducted on several HVOF coatings, including (a) Type 316L stainless steel, (b) SAM40 and (c) SAM1651 After 30 cycles in the standard GM salt-fog test, the HVOF coating of Alloy C-22 showed slight rusting (not shown), while the HVOF coatings of Type 316L stainless steel and SAM40 showed substantial corrosion. In contrast, the newer SAM1651 formulation showed no corrosion at 30 cycles. The salt fog testing ofSAM1651 was continued to almost 60 cycles with no evidence of corrosion.